PHYSICAL REVIEW LETTERS **129,** 046001 (2022)

Editors' Suggestion **Featured in Physics**

Robustness of Bilayer Hexagonal Ice against Surface Symmetry and Corrugation

Pu Yang,[1,*] Chen Zhang,[1,*] Wenyu Sun,[1] Jia Dong,[1] Duanyun Cao,[2,3,†] Jing Guo,[1,5,‡] and Ying Jiang[4,5,§]

[1]*College of Chemistry, Key Laboratory of Theoretical and Computational Photochemistry,*
Beijing Normal University, Beijing 100875, China
[2]*Beijing Key Laboratory of Environmental Science and Engineering, School of Materials Science and Engineering,*
Beijing Institute of Technology, Beijing 100081, China
[3]*Beijing Institute of Technology Chongqing Innovation Center, Chongqing 401120, China*
[4]*International Center for Quantum Materials, School of Physics, Peking University, Beijing 100871, China*
[5]*Interdisciplinary Institute of Light-Element Quantum Materials and Research Center for Light-Element Advanced Materials,*
Peking University, Beijing 100871, China

(Received 21 December 2021; accepted 7 June 2022; published 18 July 2022)

Two-dimensional (2D) bilayer hexagonal ice (BHI) is regarded as the first intrinsic 2D ice crystal. However, the robustness of such a structure or its derivatives against surface symmetry and corrugation is still unclear. Here, we report the formation of 2D BHI on gold surfaces with 1D corrugation, using noncontact atomic force microscopy. The hexagonal arrangement of the first wetting layer was visualized on the Au(110)-1 × 2 surface. Upon depositing more water molecules, the first layer would rearrange and shrink, resulting in the formation of buckled BHI. Such a buckled BHI is hydrophobic despite the appearance of dangling OH, due to the strong interlayer bonding. Furthermore, the BHI is also stable on the Au(100)-5 × 28 surface. This work reveals the unexpected generality of the BHI on corrugated surfaces with nonhexagonal symmetry, thus shedding new light on the microscopic understandings of the low-dimensional ice formation on solid surfaces or under confinement.

DOI: 10.1103/PhysRevLett.129.046001

The formation of 2D ices has been extensively reported on surfaces of either hydrophobic or hydrophilic [denoting relatively low or high water-surface binding energy compared with the water-water hydrogen (H) bond, respectively] materials [1–10], and even under nanoscale confinement [11–15]. In contrast to the structural diversity of water on hydrophilic surfaces, which is strongly surface dependent [3,4,16–19], the structure of the water-ice layer on hydrophobic surfaces is mainly dominated by the water-water H-bonding interaction, resulting in the formation of interlocked BHI (two complete hexagonal layers of water molecules). BHI is the first intrinsic 2D ice crystal (named 2D ice I), which has been confirmed both theoretically [12] and experimentally [2,10,20]. The BHI exhibits anomalously high melting temperature [9,12,21], suggesting its ubiquity even under ambient condition. It has been realized only recently that the BHI may play hidden roles in many natural processes and applied fields, such as surface wetting and ice growth [22], surface adhesion and friction [23], ultrafast water transport in 2D channels [24], etc. So far, most of the studies have been focused on flat hydrophobic surfaces with hexagonal symmetry, such as graphene [10], graphite [8] and Au(111) [2,20,25]. However, whether such a BHI structure or its derivatives can remain stable on corrugated surfaces with nonhexagonal symmetry and a different degree of hydrophobicity is still unclear, which corresponds to the key issue to generalize the application of BHI.

Recently, qPlus-based noncontact atomic force microscopy (NCAFM) [26] enables real-space imaging of interfacial water with superior resolution, such as discerning the O-H directionalities in a nearly noninvasive manner [27], identifying the atomic H-bonding skeleton [28], resolving the single ion hydrates [29] and revealing the growth mechanism of a low-dimensional ice by probing the edge structures [20]. In this Letter, using NCAFM in combination with density functional theory (DFT) calculations, we visualized the formation of hydrophobic BHI on both Au(110)-1 × 2 and Au(100)-5 × 28 surfaces, showing periodic 1D reconstruction with the spacing of 8.2 and 14.4 Å, respectively. Our findings indicate the robustness of BHI against the surface morphology and the degree of hydrophobicity.

The Au(110) surface is known to reconstruct into the (1 × 2) surface because of missing rows along the $[1\bar{1}0]$ direction [Fig. 1(a)]. High-resolution STM topography of the Au(110)-1 × 2 surface shows the ordered array of close-packed gold rows along the $[1\bar{1}0]$ direction with the spacing of 8.20 Å [Fig. 1(b)]. Depositing water molecules on the Au(110) surface at 120 K leads to the formation of monolayer ice with a thickness of about 1.2 Å [Fig. 1(c)]. The water layer is visualized as ordered zigzag chains above the topmost gold rows accompanied with some isolated bright protrusions in the close-up STM image [Fig. 1(d)]. In contrast, the AFM frequency shift (Δf)

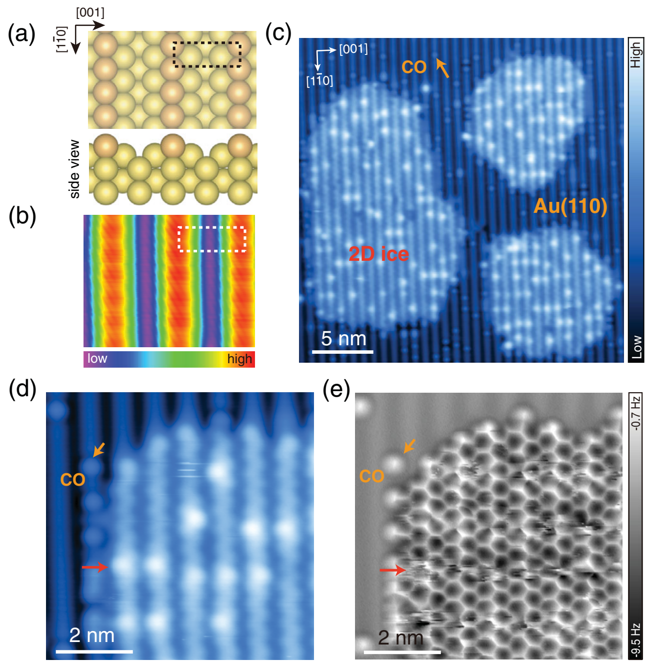

FIG. 1. (a) Schematic model of the reconstructed Au(110)-1 × 2 surface. (b) Atomic-resolution STM image of Au(110)-1 × 2 surface (set point: 10 mV, 1 nA; size: 2.3 nm × 1.8 nm). Dash rectangles represent the 1 × 2 unit cell. (c),(d) Overview (c) and close-up STM (d) images of monolayer ice (set point: 100 mV, 5 pA). (e) Constant height AFM image of the same region as in (d), recorded at a tip height of −70 pm. The red arrows indicate the scratching noises in the AFM image (e) induced by the disturbance of the CO-terminated tip on the higher-lying water molecules (d). The tip height of the experimental AFM image is defined in the Materials and Methods. The oscillation amplitude of the AFM image is 100 pm.

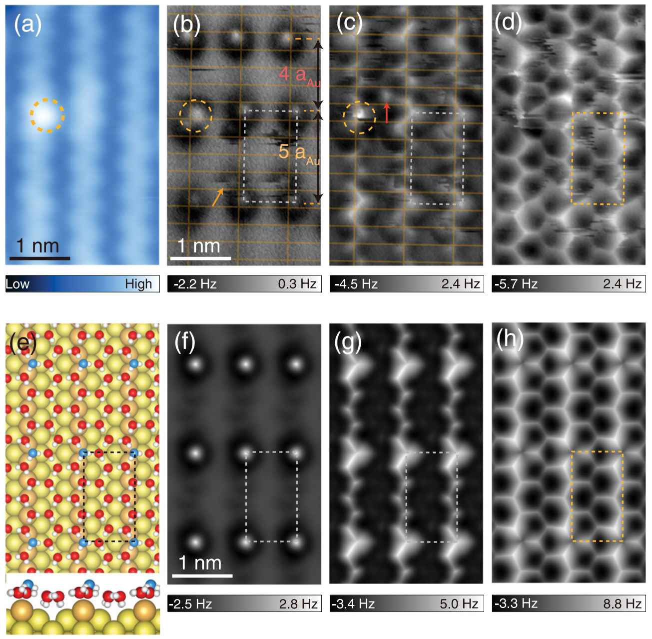

FIG. 2. (a) Close-up STM image (set point: 100 mV, 5 pA) of a monolayer ice island on Au(110)-1 × 2 surface. (b)–(d) Height dependent AFM imaging at tip heights of 100 pm (b), −50 pm (c), −130 pm (d). The isolated H-up water molecule on the topmost gold rows and flat-lying water molecule in the trench is highlighted by yellow circles and red arrow, respectively. The yellow arrow in (b) indicates the jump of the flat-lying water molecule from near-top to near-bridge sites. (e) Top and side views of the atomic model of monolayer ice. Au, H, and O atoms are denoted as yellow, white, and red spheres, while water molecules at the bridge site are highlighted by blue spheres. (f)–(h) Simulated AFM images acquired at tip heights of 11.2 Å (f), 10.1 Å (g), 9.6 Å (h). The dash rectangles indicate the 5 × 2 unit cell. The tip heights of experimental and simulated AFM images are defined in the Materials and Methods.

image exhibits much higher resolution, clearly resolving the ordered hexagonal structure of the water layer (lattice constant, 4.70 ± 0.02 Å) [Fig. 1(e)].

Then we performed the systematic AFM imaging at different tip heights so as to capture more detailed features of the H-bonding network. At a large tip height, the water layer is visualized as an ordered array of bright protrusions [Fig. 2(b) and Fig. S1 [30]], in which the brighter ones correspond to the isolated bright protrusions shown in the STM image [yellow dashed circles in Figs. 2(a) and 2(b)] while the ones with smaller contrasts are invisible in the STM image [Fig. 2(a)]. Those bright protrusions appear on the topmost gold rows and are mainly distributed with the nearest neighboring distances of 4 a_{Au} or 5 a_{Au} [$a_{\mathrm{Au}} = 288$ pm, denoting the nearest neighboring distance of the topmost gold atoms on Au(110)] [Fig. 2(b) and Fig. S1 [30]]. When the AFM image acquired at a large tip height is overlaid with the Au(110)-1 × 2 atomic lattice [Fig. 2(b) and Fig. S2 [30]], we notice that the bright protrusions reside exactly at the near-bridge sites of the rows. Upon decreasing the tip height, water molecules adsorbed on the topmost gold rows appear in a zigzag arrangement [Fig. 2(c)]. There are five (six) water molecules residing within the periodic distance of 4 a_{Au} (5 a_{Au}) (Fig. S1 [30]). At the small tip height, where the short-range Pauli repulsion force is dominant [39,40], the lowest-lying water molecules in the trenches are visualized and the water layer exhibits a honeycomb structure [Fig. 2(d)].

Based on the high-resolution AFM images, we construct a hexagonal water layer with the periodicity of Au(110)-5 × 2, which contains 12 water molecules in each unit cell [dash rectangle in Fig. 2]. DFT calculations reveal the most stable H-bonding arrangement of the monolayer hexagonal ice, in which the water molecules adsorbed on the topmost gold rows show the flat-lying configuration and those in the trenches have the OH pointing toward the low-coordinated gold atoms, so as to enhance the bonding with the substrate [Fig. 2(e) and Fig. S3 [30]]. What is more, the flat-lying water molecules adsorb periodically on the bridge sites of the gold rows [highlighted by blue spheres in Fig. 2(e)], which are about 1 Å higher than other flat-lying water molecules residing at the near-top sites, due to the weaker

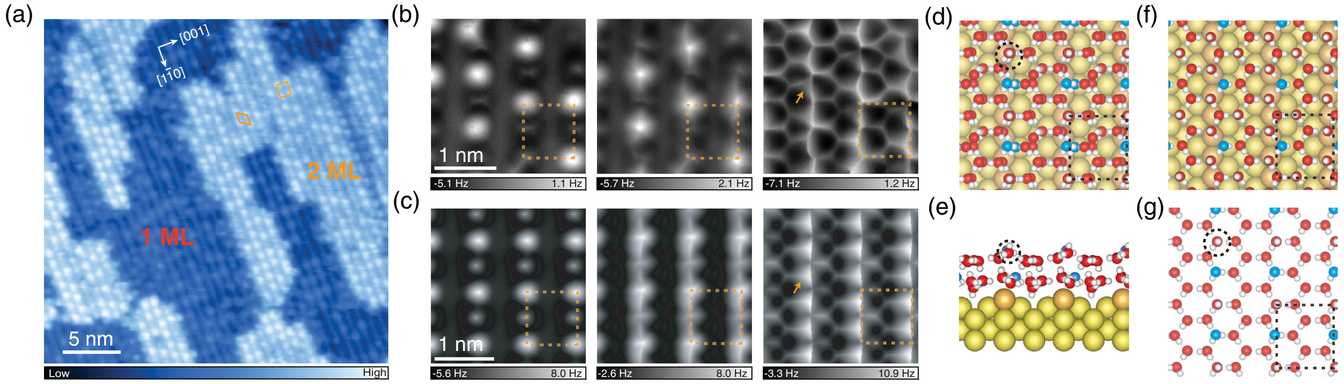

FIG. 3. (a) Overview STM image (set point: 300 mV, 5 pA) of buckled BHI on the Au(110)-1×2 surface. The yellow rhombus and rectangle represent the hexagonal and rectangle arrangements of bilayer ice, respectively. (b) Height dependent AFM imaging at tip heights of 320 pm (left), 270 pm (middle), 200 pm (right). (c) Simulated AFM images acquired at tip heights of 14.2 Å (left), 13.6 Å (middle), 13.1 Å (right). (d),(e) Top and side views of the calculated structure of buckled BHI. (f),(g) First layer (f) and second layer (g) structure. The black dash circles in (d),(e),(g) represent the H-up water molecules in the second layer. The yellow and black rectangles in (b)–(g) indicate the 3×2 unit cell.

interaction with the substrate. Such a small height difference is indistinguishable in the STM images, but can be clearly resolved in the AFM images at large tip heights. The AFM simulations at different tip heights [Figs. 2(f)–2(h)] nicely reproduce the experimental observations [Fig. 2(b)–2(d)], thus confirming the validity of the DFT model [Fig. 2(e)].

We have also carried out the DFT calculations and AFM simulations on a larger 8×2 unit cell containing 20 water molecules, which agree well with the experimental findings that the protrusions with the distance of $4\ a_{\mathrm{Au}}$ are residing at opposite sides of the topmost gold rows (Fig. S4 [30]). The bright protrusions in the STM images denote water molecules in H-up configurations (one OH of water is dangling), which is supported by DFT calculations, AFM simulations and force-curve measurements (Fig. S5 [30]). Such a monolayer ice might be helpful for the multilayer ice growth, since the H-up configurations are believed to facilitate second layer water adsorption. We note that the water-surface interaction (315 meV) is only slightly weaker than the water-water interaction (387 meV) for the monolayer water on Au(110) (Fig. S6 [30]). Therefore, the Au(110) surface lies actually at the boundary between the hydrophobic and hydrophilic regimes. The interaction of water with Au(110) is much stronger than that of Au(111) surface (185 meV) [41] due to the low coordination of Au(110) surface atoms.

As increasing the water coverage, we observe the wetting of the first water layer on the surface and the growth of second ice layer [Fig. 3(a) and Fig. S7 [30]]. The high-resolution STM image shows that the second layer ice is characterized as bright features arranged in a hexagonal, or a rectangular ordering with a period of about 0.890 nm ($3\ a_{\mathrm{Au}}$) [Fig. 3(a) and Fig. S7 [30]]. We also observed the occasionally missing of the bright features, which induces the local disordering of the water layer.

In order to further explore the atomic structures of the bilayer ice, we perform the height-dependent AFM imaging with a CO-functionalized tip [Fig. 3(b)]. At the large tip height, the bright features shown in the STM image are visualized as prominent round protrusions accompanied with small faded features residing between them [Fig. 3(b), left panel]. When the tip is approached to the water layer, the brighter protrusions evolve into asymmetric bright features with sharp lines toward the lower-lying water molecules [Fig. 3(b), middle panel]. However, water molecules sitting in the trenches still could not be resolved, indicating the formation of buckled bilayer ice following the topography of the substrate. At the smallest tip height, we observe the hexagonal H-bonding network [Fig. 3(b), right panel], in which the bright protrusions fade out and the trianglelike bright features appear [yellow arrow in Fig. 3(b), right panel], due to the deflection of the CO molecule. The lattice constant of this BHI is around 4.42 ± 0.08 Å along the $[1\bar{1}0]$ direction of the substrate, which is heavily compressed compared with the original monolayer ice and approaches the lattice constant of ice I_h in the (0001) plane, thus further validating the buckled nature of this double-layer ice.

Based on the rectangle unit cell shown in Fig. 3(b), we construct the 3×2 periodic BHI on the Au(110)-1×2 surface, which contains eight water molecules per layer. We have considered a number of possible structures of the BHI (see the details in Figs. S8–S14 [30]). The structural confirmation of the buckled BHI is based on the following two aspects: (1) energy minimization; (2) agreements between the experimental submolecular-resolution AFM images and the AFM simulations. Figures 3(d) and 3(e) show the most stable DFT calculated structure of the BHI and the corresponding AFM simulations [Fig. 3(c)] at different tip heights, which nicely reproduce the experimental results [Fig. 3(b)].

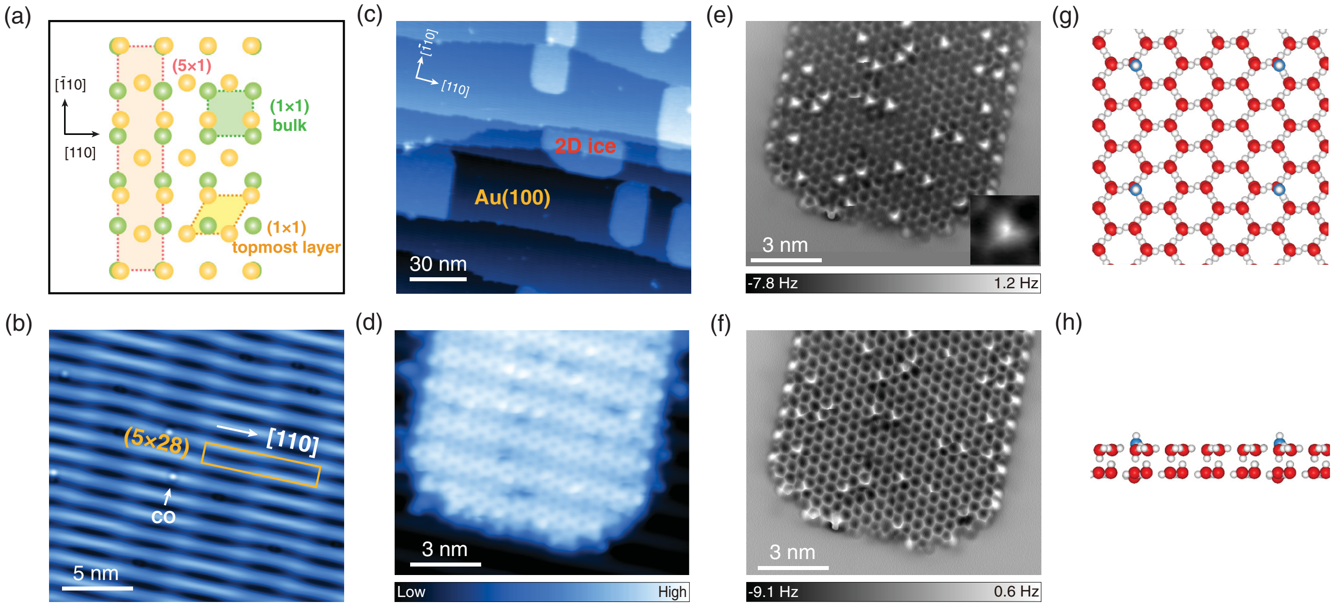

FIG. 4. (a) Schematic model of the reconstructed hexagonal array of the topmost layer (yellow spheres) on the bulk Au(100) surface with square symmetry (green spheres). (b) STM topography of reconstructed Au(100) surface, showing 5 × 28 reconstruction (set point: 100 mV, 50 pA). (c) Overview STM image of 2D ice on reconstructed Au(100) surface (set point: 1 V, 5 pA). (d)–(f) High resolution STM image (set point: 100 mV, 4 pA) (d) and height dependent AFM imaging at tip heights of 320 pm (e) and 290 pm (f). Inset of (e): close-up AFM image of a H-up water in second layer (size: 0.8 nm × 0.8 nm). (g),(h) Top and side views of the flat BHI model with isolated dangling OH (blue spheres).

The bright protrusions with larger and smaller contrasts shown in the AFM image at large tip height represent H-up and flat-lying water molecules in the upper layer, respectively, which are not H bonded with the underneath water molecules and thus lie further away from the surface than the others [Figs. 3(d) and 3(e)]. In order to give a clear view of the bilayer ice, we display the structures of the first and second layers separately in Figs. 3(f) and 3(g). At the first layer, the water molecules in the trenches are arranged as H-up/flat/H-down/flat configurations sequentially and the water molecules adsorbed on the gold rows as H-up and flat-lying configurations alternatively [see the unit cell shown in Fig. 3(f)]. At the second layer, the water molecules above the trenches are all H bonded with the first layer ice either in flat or H-down configurations [Fig. 3(g)]. In contrast, only half of the water molecules above the gold rows are H bonded with the underneath water molecules, forming buckled bilayer ice. The bilayer ice with hexagonal ordering [see Fig. 3(a)] was also reproduced by positioning the H-up molecules on different sites of adjacent rows (Fig. S8 [30]).

Because of the moderate interaction of water with the corrugated Au(110) surfaces, the water molecules in the first layer could easily rearrange and flip upon the growth of the second layer ice, resulting in the formation of buckled BHI ($a_{2D} = 4.42 \pm 0.08$ Å). Though the underneath of the ordered second layer ice is invisible in the experiment, we find the appearance of local defects at the regions of structural transition from monolayer to bilayer ice (Fig. S15 [30]), which is induced by the incommensurability between the original and reconstructed first hexagonal layer.

Further increasing the water coverage, we observed the formation of multilayer ice islands on the bilayer ice film (Fig. S16 [30]), indicating that the buckled BHI is very stable and actually hydrophobic. This is in contrast with the previously proposed layer-by-layer growth model of multilayer ice on a corrugated Cu(511) surface [42], although the similar buckled BHI was observed. A close inspection of the buckled BHI reveals that six out of the eight water molecules in the unit cell of the second layer are fully H bonded with the others and the displacement between the two layers further enhances the interlayer H-bonding interaction [Figs. 3(d)–3(g)]. Therefore, the interlocked feature is largely preserved in the buckled BHI on Au(110) and there is a limited number density of water molecules that could act as H-bonding donors (dangling OHs) or acceptors to form additional H bonds, thus resembling the hydrophobic character of flat BHI on Au(111) and prohibiting the subsequent layer-by-layer wetting growth.

In order to further explore the generality of BHI on corrugated surfaces, we investigated the ice growth on the Au(100) surface, which tends to reconstruct into quasi-hexagonal surface with nanoscale 1D constraint [Fig. 4(a)] [43,44]. The STM image of the Au(100) surface shows the characteristic 1D fringes with the spacing of 14.4 Å, exhibiting a 5 × 28 reconstruction in the topmost layer [Fig. 4(b)]. We find the formation of a 2D hexagonal ice on reconstructed Au(100) surface at 120 K with a thickness of around 2.6 Å [Fig. 4(c)–4(f)], which looks similar to the flat

BHI formed on Au(111) surfaces. Most of the molecules in the upper layer show the similar contrast except for some isolated triangle pyramidal shaped bright protrusions, which are ascribed to H-up water molecules [Fig. 4(e) and Fig. S17 [30]]. These observations indicate that the reconstructed Au(100) surface with strong 1D constraint also allows the formation of flat BHI with some isolated dangling OH [Figs. 4(g) and 4(h)]. Moreover, the BHI shows the same lattice constant (5.04 ± 0.08 Å) as that on the Au(111) surface [20], which is not in perfect registry with the underneath quasihexagonal surface (Fig. S18 [30]), indicating the robustness of BHI.

In conclusion, using NCAFM in combination with DFT calculations, we found the formation of BHI on reconstructed Au(110) and Au(100) surfaces. These results reveal the robustness of BHI on nonhexagonal and corrugated substrates with a vastly different degree of hydrophobicity (Fig. S6 [30]), thus shedding new light on the microscopic understandings of the low-dimensional ice formation on solid surfaces or under confinement. The BHI seems quite flexible to make minimal adjustment to accommodate different substrates, which we believe will stimulate the wide application of BHI as a new type of 2D material in the future, such as anti-icing, superlubrication, and emergent quantum matters. Considering that III-V, II-VI, and I-VII semiconductors have been theoretically predicted to form the BHI-like structure at the 2D limit [45], we expect that BHI-like structure might be general for a large family of tetrahedrally structured materials with vastly different bonding strength.

We are thankful for the financial support from the National Key R&D Program of China under Grant No. 2021YFA1400501, the National Natural Science Foundation of China under Grants No. 21902013, No. 91961118, and Beijing Natural Science Foundation under Grant No. 1202016 and the Fundamental Research Funds for the Central Universities. J. G. acknowledges support from the National Program for Support of Top-notch Young Professionals. D. C. acknowledges support from the National Postdoctoral Program for Innovative Talents under Grant No. BX2021040, the China Postdoctoral Science Foundation under Grant No. 2021M690408 and the Beijing Institute of Technology Research Fund Program for Young Scholars. We are thankful for the computational resources provided by the Beijing Super Cloud Computing Center, the High-performance Computing Platform of Beijing Institute of Technology Chongqing Innovation Center and the TianHe-1A supercomputer.

---

[*] These authors contributed equally to this work.

[†] Corresponding author.
dycao@bit.edu.cn

[‡] Corresponding author.
jguo1294@bnu.edu.cn

[§] Corresponding author.
yjiang@pku.edu.cn

[1] A. Hodgson and S. Haq, Surf. Sci. Rep. **64**, 381 (2009).

[2] G. Corem, P. R. Kole, J. D. Zhu, T. Kravchuk, J. R. Manson, and G. Alexandrowicz, J. Phys. Chem. C **117**, 23657 (2013).

[3] S. Nie, P. J. Feibelman, N. C. Bartelt, and K. Thurmer, Phys. Rev. Lett. **105**, 026102 (2010).

[4] S. Maier, B. A. Lechner, G. A. Somorjai, and M. Salmeron, J. Am. Chem. Soc. **138**, 3145 (2016).

[5] C. Lin, N. Avidor, G. Corem, O. Godsi, G. Alexandrowicz, G. R. Darling, and A. Hodgson, Phys. Rev. Lett. **120**, 076101 (2018).

[6] M. Mehlhorn and K. Morgenstern, Phys. Rev. Lett. **99**, 246101 (2007).

[7] M. Odelius, M. Bernasconi, and M. Parrinello, Phys. Rev. Lett. **78**, 2855 (1997).

[8] L. Lupi, N. Kastelowitz, and V. Molinero, J. Chem. Phys. **141**, 18C508 (2014).

[9] C. Zhu, Y. Gao, W. Zhu, J. Jiang, J. Liu, J. Wang, J. S. Francisco, and X. C. Zeng, Proc. Natl. Acad. Sci. U.S.A. **116**, 16723 (2019).

[10] G. A. Kimmel, J. Matthiesen, M. Baer, C. J. Mundy, N. G. Petrik, R. S. Smith, Z. Dohnálek, and B. D. Kay, J. Am. Chem. Soc. **131**, 12838 (2009).

[11] K. Xu, P. Cao, and J. R. Heath, Science **329**, 1188 (2010).

[12] K. Koga, X. C. Zeng, and H. Tanaka, Phys. Rev. Lett. **79**, 5262 (1997).

[13] G. Algara Siller, O. Lehtinen, F. C. Wang, R. R. Nair, U. Kaiser, H. A. Wu, A. K. Geim, and I. V. Grigorieva, Nature (London) **519**, 443 (2015).

[14] J. Chen, G. Schusteritsch, C. J. Pickard, C. G. Salzmann, and A. Michaelides, Phys. Rev. Lett. **116**, 025501 (2016).

[15] P. Bampoulis, V. J. Teernstra, D. Lohse, H. J. W. Zandvliet, and B. Poelsema, J. Phys. Chem. C **120**, 27079 (2016).

[16] J. Carrasco, A. Michaelides, M. Forster, S. Haq, R. Raval, and A. Hodgson, Nat. Mater. **8**, 427 (2009).

[17] T. Yamada, S. Tamamori, H. Okuyama, and T. Aruga, Phys. Rev. Lett. **96**, 036105 (2006).

[18] J. Chen, J. Guo, X. Meng, J. Peng, J. Sheng, L. Xu, Y. Jiang, X. Z. Li, and E. G. Wang, Nat. Commun. **5**, 4056 (2014).

[19] D. Halwidl *et al.*, Nat. Mater. **15**, 450 (2016).

[20] R. Ma *et al.*, Nature (London) **577**, 60 (2020).

[21] K. Koga, H. Tanaka, and X. C. Zeng, Nature (London) **408**, 564 (2000).

[22] J. Liu, C. Zhu, K. Liu, Y. Jiang, Y. Song, J. S. Francisco, X. C. Zeng, and J. Wang, Proc. Natl. Acad. Sci. U.S.A. **114**, 11285 (2017).

[23] L. Chen and L. Qian, Friction **9**, 1 (2021).

[24] B. Radha *et al.*, Nature (London) **538**, 222 (2016).

[25] D. Stacchiola, J. B. Park, P. Liu, S. Ma, F. Yang, D. E. Starr, E. Muller, P. Sutter, and J. Hrbek, J. Phys. Chem. C **113**, 15102 (2009).

[26] F. J. Giessibl, Rev. Mod. Phys. **75**, 949 (2003).

[27] J. Peng *et al.*, Nat. Commun. **9**, 122 (2018).

[28] A. Shiotari and Y. Sugimoto, Nat. Commun. **8**, 14313 (2017).

[29] J. Peng *et al.*, Nature (London) **557**, 701 (2018).

[30] See Supplemental Material at http://link.aps.org/supplemental/10.1103/PhysRevLett.129.046001 for materials and methods, more experimental data, theoretical

calculation and simulation results, and further discussion, which includes Refs. [31–38].

[31] I. Horcas, R. Fernández, J. M. Gómez Rodríguez, J. Colchero, J. Gómez Herrero, and A. M. Baro, Rev. Sci. Instrum. **78**, 013705 (2007).

[32] G. Kresse and J. Hafner, Phys. Rev. B **47**, 558 (1993).

[33] G. Kresse and J. Furthmüller, Phys. Rev. B **54**, 11169 (1996).

[34] G. Kresse and D. Joubert, Phys. Rev. B **59**, 1758 (1999).

[35] J. Klimeš, D. R. Bowler, and A. Michaelides, J. Phys. Condens. Matter **22**, 022201 (2010).

[36] J. Klimeš, D. R. Bowler, and A. Michaelides, Phys. Rev. B **83**, 195131 (2011).

[37] P. Hapala, R. Temirov, F. S. Tautz, and P. Jelínek, Phys. Rev. Lett. **113**, 226101 (2014).

[38] J. E. Sader and S. P. Jarvis, Appl. Phys. Lett. **84**, 1801 (2004).

[39] P. Hapala, G. Kichin, C. Wagner, F. S. Tautz, R. Temirov, and P. Jelínek, Phys. Rev. B **90**, 085421 (2014).

[40] L. Gross, F. Mohn, N. Moll, P. Liljeroth, and G. Meyer, Science **325**, 1110 (2009).

[41] A. Dong, L. Yan, L. Sun, S. Yan, X. Shan, Y. Guo, S. Meng, and X. Lu, ACS Nano **12**, 6452 (2018).

[42] C. Lin, G. Corem, O. Godsi, G. Alexandrowicz, G. R. Darling, and A. Hodgson, J. Am. Chem. Soc. **140**, 15804 (2018).

[43] D. G. Fedak and N. A. Gjostein, Surf. Sci. **8**, 77 (1967).

[44] S. Bengió, V. Navarro, M. A. González-Barrio, R. Cortés, I. Vobornik, E. G. Michel, and A. Mascaraque, Phys. Rev. B **86**, 045426 (2012).

[45] M. C. Lucking, W. Xie, D. H. Choe, D. West, T. M. Lu, and S. B. Zhang, Phys. Rev. Lett. **120**, 086101 (2018).